

Image Denoising Using Global and Local Circulant Representation

Zhaoming Kong, Xiaowei Yang, and Jiahuan Zhang

Abstract—The proliferation of imaging devices and countless image data generated every day impose an increasingly high demand on efficient and effective image denoising. In this paper, we establish a theoretical connection between principal component analysis (PCA) and the Haar transform under circulant representation, and present a computationally simple denoising algorithm. The proposed method, termed Haar-tSVD, exploits a unified tensor singular value decomposition (t-SVD) projection combined with Haar transform to efficiently capture global and local patch correlations. Haar-tSVD operates as a one-step, parallelizable plug-and-play denoiser that eliminates the need for learning local bases, thereby striking a balance between denoising speed and performance. Besides, an adaptive noise estimation scheme is introduced to improve robustness according to eigenvalue analysis of the circulant structure. To further enhance the performance under severe noise conditions, we integrate deep neural networks with Haar-tSVD based on the established Haar-PCA relationship. Experimental results on various denoising datasets demonstrate the efficiency and effectiveness of proposed method for noise removal. Our code is publicly available at <https://github.com/ZhaomingKong/Haar-tSVD>.

Index Terms—Efficient image denoising, circulant representation, tensor-SVD projection, Haar transform, real-world datasets.

I. INTRODUCTION

The rapid development of modern imaging systems and technologies has significantly enriched the information captured and conveyed by images, delivering a more faithful representation for real scenes. However, images are inevitably corrupted by noise during acquisition and transmission, which can severely degrade the visual quality of acquired data. Therefore, effective image denoising remains a fundamental task in many applications, including feature extraction, object tracking, and medical diagnosis [1], [2].

Many state-of-the-art image denoising techniques weigh highly on deep neural network (DNN) architectures, which are usually trained on datasets containing clean and noisy image pairs. For example, Zhang et al. [3] incorporated batch normalization (BN) [4], rectified linear unit (ReLU) [5] and residual learning [6] into the convolutional neural network (CNN) model. Chen et al. [7] considered an efficient activation free network. Zamir et al. [8] introduced transformer [9] to capture long-range image pixel interactions. While the data-driven models have shown impressive performance for image

Z. Kong and X. Yang are with the School of Software Engineering, South China University of Technology, Guangzhou, 510006, China (e-mail: kong.zm@mail.scut.edu.cn; xwyang@scut.edu.cn).

J. Zhang is with the Department of Clinical Laboratory Medicine, Guangdong Provincial People's Hospital, Southern Medical University, Guangzhou, 510000, China (email: zhangjiahuan@gdph.org.cn).

restoration, their performance may degrade sharply when the test images do not match the distribution of the current scene. Besides, collecting high-quality data is time-consuming and expensive, and the platform required for training and inference may be inaccessible to ordinary users and researchers.

Therefore, it is interesting to devise denoising methods with less dependence on ground-truth data and low computational complexity. As an alternative to DNN models, the classic patch-based denoising framework still shows competitive performance in various tasks [10]. In general, related works filter out noise based solely on the input noisy observation with different regularization terms and image priors [11], [12]. The representative BM3D method [13] integrated the NLSS characteristic of natural images [14], sparse representation [15] and transform-domain techniques [16] into a subtle paradigm. Gu et al. [17] replaced the sparsity constraint with the low-rank assumption. Xu et al. [18] employed the Maximum A-Posterior (MAP) estimation technique [19] and proposed a trilateral weighted sparse coding scheme.

Despite steady progress, existing methods still face several inherent limitations [20], including the need for solving complex optimization problems in the test phase, reliance on manually tuned parameters, and insufficient exploitation of auxiliary information. To circumvent these issues and achieve a balance between denoising performance and computational resources, we take advantage of the circulant representation [21], [22] and propose Haar-tSVD to capture the local and nonlocal similarity. Furthermore, we investigate an effective combination of DNNs and the proposed denoiser to utilize both external information and internal image structures. Following the patch-based denoising paradigm, the proposed method is distinguished by several characteristics.

First, we exploit the global circulant representation to model patch-level correlation, which can be efficiently captured by a pair of shared t-SVD bases. We then extend this global patch circulant structure to a local group-level circulant formulation, thereby revealing an intrinsic connection between the Haar transform and PCA. The resulting global-local circulant correlation leads to a unified integration of t-SVD and Haar bases, eliminating the need for local transform learning, yielding a parallelizable and plug-and-play denoiser. Besides, to improve the adaptability and avoid manual parameter tuning, we develop an adaptive variant termed A-Haar-tSVD, which adjusts the noise estimation value based on the eigenvalue characteristics of circulant structures. Moreover, to improve robustness under severe noise, we propose fusing DNNs with the established Haar-PCA link to leverage both external information and intrinsic image features.

Our main contributions can be summarized as follows:

- **Unified bases:** We propose to leverage the circulant representation to capture both the intra- and inter-correlations among image patches. Furthermore, by building the connection between the Haar transform and PCA via the eigenvalue decomposition (EVD) of the circulant structure, we demonstrate that the global-local circulant similarity can be efficiently exploited by a unified t-SVD projection and Haar transform.
- **Adaptive scheme:** We develop an adaptive scheme to enhance the flexibility and robustness of the proposed method by exploring a CNN-based noise estimator alongside eigenvalue characteristics of circulant structures. To reduce computational overhead, a fast implementation is achieved through parallel programming techniques.
- **Enhancement strategy:** We leverage the established Haar-PCA relationship and introduce a learning-based enhancement strategy that integrates a data-driven module with the proposed denoiser, improving robustness and denoising performance in challenging scenarios.
- **Diverse datasets:** We evaluate the applicability of the proposed method across different real-world denoising tasks such as images, videos and hyperspectral imaging (HSI). Experiments demonstrate the competitive performance of the proposed method in terms of both effectiveness and efficiency.

The rest of the paper is structured as follows. Section II summarizes related works. Section III describes the proposed Haar-tSVD denoising method and its variants in detail. Section IV presents datasets, experimental settings and results. Besides, discussions of the ablation studies are included in this section. Section V concludes this work.

II. RELATED WORKS

A. Symbols and Notations

We follow the tensor notations in [23] for image representation. Vectors and matrices are first- and second-order tensors, denoted by bold lowercase letters \mathbf{a} and bold capital letters \mathbf{A} , respectively. A higher order tensor is denoted by calligraphic letters, e.g., \mathcal{A} . An N th-order tensor is denoted as $\mathcal{A} \in \mathbb{R}^{I_1 \times I_2 \times \dots \times I_N}$. The n -mode product of a tensor \mathcal{A} by a matrix $\mathbf{U} \in \mathbb{R}^{P_n \times I_n}$, denoted by $\mathcal{A} \times_n \mathbf{U}$ is also a tensor. The mode- n unfolding of \mathcal{A} is denoted by $\mathbf{A}_{(n)}$.

B. Patch-based Framework

Patch-based denoisers typically exploit the NLSS property through three stages: grouping, collaborative filtering, and aggregation, as illustrated in Fig. 1. For a reference patch $\mathcal{P}_n \in \mathbb{R}^{ps \times ps \times c}$, the grouping step stacks K similar patches within a local window W into a 4D group $\mathcal{G}_n \in \mathbb{R}^{ps \times ps \times c \times K}$ based on certain patch-matching criteria [24]–[26]. Collaborative filtering then estimates the underlying clean group via

$$\hat{\mathcal{G}}_c = \arg \min_{\mathcal{G}_c} \|\mathcal{G}_n - \mathcal{G}_c\|_F^2 + \rho \cdot \Psi(\mathcal{G}_c), \quad (1)$$

where $\Psi(\cdot)$ encodes prior knowledge. Finally, the clean patches in $\hat{\mathcal{G}}_c$ are aggregated back to their original locations to suppress residual noise.

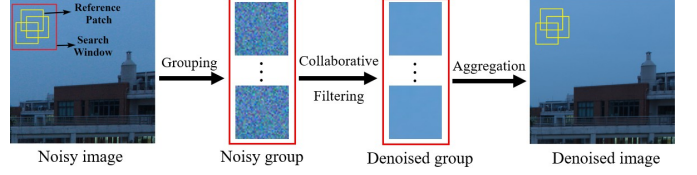


Fig. 1. Illustration of the patch-based framework for traditional denoisers.

C. Circulant Representation and t-SVD for Image Denoising

Recently, circulant structure and representation [22], [27], [28] has been utilized for image restoration due to its effectiveness of exploring redundancy and encoding the inner structure of an image patch by cyclic shift. The block circulant representation (BCR) [22] of an image patch $\mathcal{P} \in \mathbb{R}^{ps \times ps \times c}$ models patch-level redundancy as

$$bcirc(\mathcal{P}) = \begin{pmatrix} \mathcal{P}^{(1)} & \mathcal{P}^{(c)} & \dots & \mathcal{P}^{(2)} \\ \mathcal{P}^{(2)} & \mathcal{P}^{(1)} & \dots & \mathcal{P}^{(3)} \\ \vdots & \vdots & \ddots & \vdots \\ \mathcal{P}^{(c)} & \mathcal{P}^{(c-1)} & \dots & \mathcal{P}^{(1)} \end{pmatrix}, \quad (2)$$

where $\mathcal{P}^{(i)} = \mathcal{P}(:, :, i)$ denotes the i -th frontal slice, and $bcirc(\mathcal{P}) \in \mathbb{R}^{psc \times psc}$ is a block circulant matrix. This representation preserves the patch structure while capturing inter-slice correlations, making it well suited for multi-dimensional image data. Moreover, explicit construction of BCR is unnecessary, since block circulant operations can be efficiently implemented via the tensor t-product [29], [30].

Definition II.1 (T-product). Suppose $\mathcal{A} \in \mathbb{R}^{n_1 \times m \times n_3}$ and $\mathcal{B} \in \mathbb{R}^{m \times n_2 \times n_3}$, then the t-product $\mathcal{C} = \mathcal{A} * \mathcal{B} \in \mathbb{R}^{n_1 \times n_2 \times n_3}$ is defined as

$$bcirc(\mathcal{C}) = bcirc(\mathcal{A})bcirc(\mathcal{B}). \quad (3)$$

Equ. (3) can be efficiently computed in the Fourier domain

$$\mathcal{C}_F^{(i)} = \widehat{\mathcal{A}}^{(i)} \widehat{\mathcal{B}}^{(i)}, \quad i = 1, 2, \dots, m, \quad (4)$$

where $\widehat{\mathcal{A}}$ is obtained by applying the fast Fourier transform (FFT) along the third mode of \mathcal{A} via

$$\widehat{\mathcal{A}} = \mathcal{A} \times_3 \mathbf{W}_{FFT}, \quad (5)$$

where \mathbf{W}_{FFT} refers to the FFT matrix. Then the popular t-SVD [30] can be defined based on the t-product.

Definition II.2 (T-SVD). For $\mathcal{A} \in \mathbb{R}^{n_1 \times n_2 \times n_3}$, its t-SVD decomposition is given by

$$\mathcal{A} = \mathcal{U} * \mathcal{S} * \mathcal{V}^T, \quad (6)$$

where $\mathcal{U} \in \mathbb{R}^{n_1 \times n_1 \times n_3}$ and $\mathcal{V} \in \mathbb{R}^{n_2 \times n_2 \times n_3}$ are orthogonal tensors, and the entries in $\mathcal{S} \in \mathbb{R}^{n_1 \times n_2 \times n_3}$ can be viewed as singular values or coefficients of \mathcal{A} .

t-SVD has proven effective for denoising [22], [31], [32], by exploring the block circulant structure of image patches, alleviating tensor imbalance issues [33], and sharing properties with matrix-based formulations. However, existing t-SVD-based methods typically require iterative optimization and local basis learning during the test phase. This motivates the design of a simple and effective denoising scheme with t-SVD and circulant representation.

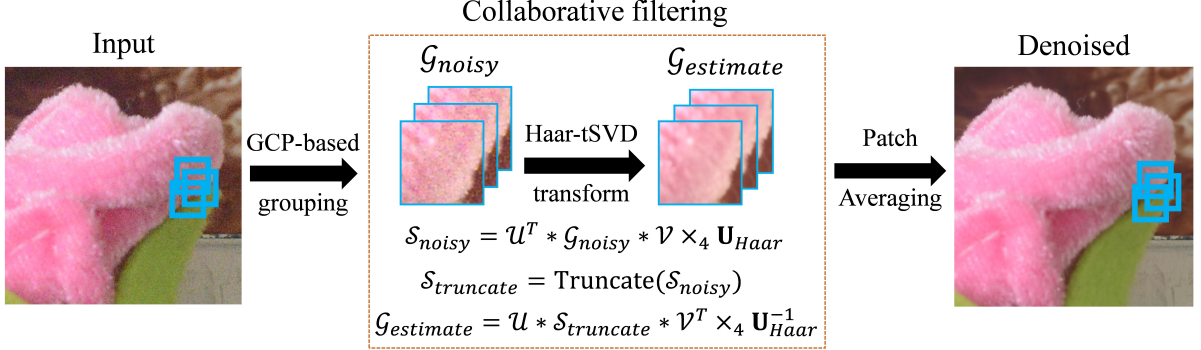


Fig. 2. Flowchart of the proposed Haar-tSVD method. It is a one-step filtering algorithm built upon global and local circulant representation.

D. Haar Transform

As a popular transformation in image filtering [34], [35], the Haar transform belongs to the wavelet family, which is derived from the Haar matrix [36]. Specifically, starting from a simple 2×2 Haar transformation matrix

$$\mathbf{H}_2 = \frac{1}{\sqrt{2}} \begin{bmatrix} 1 & 1 \\ 1 & -1 \end{bmatrix}. \quad (7)$$

We can define the general $2N \times 2N$ Haar matrix by

$$\mathbf{H}_{2N} = \frac{1}{\sqrt{2}} \begin{bmatrix} \mathbf{H}_N \otimes [1, 1] \\ \mathbf{I}_N \otimes [1, -1] \end{bmatrix}, \quad (8)$$

where $\mathbf{I}_N \in \mathbb{R}^{N \times N}$ denotes the identity matrix and \otimes represents the Kronecker product [23]. The Haar matrix plays an important role in the analysis of the localized features due to its simplicity and orthogonality. In this paper, we study the Haar transform from the perspective of circulant structure, and discuss how it can be efficiently and effectively integrated into the patch-based denoising framework.

III. METHOD

In this section, we first provide a detailed description of the proposed Haar-tSVD method, whose flowchart is depicted in Fig. 2. We then introduce its adaptive variant and the corresponding robust enhancement strategy.

A. Searching Similar Patches

Directly computing the Euclidean distance between two patches $\mathcal{P}_i, \mathcal{P}_j \in \mathbb{R}^{ps \times ps \times 3}$ is both time-consuming and sensitive to noise. Based on the observation that the green channel generally has higher SNR [37], we adopt a GCP-based patch-matching method [38], which computes the distance d_{ij} between two patches via

$$d_{ij} = \begin{cases} \|\mathcal{P}_i^G - \mathcal{P}_j^G\|, & \|\mathcal{P}_i^G\| \geq \max\left(\frac{1}{\gamma} \|\mathcal{P}_i^R\|, \frac{1}{\gamma} \|\mathcal{P}_i^B\|\right) \\ \|\mathcal{P}_i^{avg} - \mathcal{P}_j^{avg}\|, & \text{otherwise,} \end{cases} \quad (9)$$

where $\mathcal{P}^R, \mathcal{P}^G$ and \mathcal{P}^B represents the R, G and B channels of an image patch \mathcal{P} , respectively. \mathcal{P}^{avg} is the average value of RGB channels. The weight parameter γ is used to measure the importance of the green channel. Similar to [38], we empirically set $\gamma = 1.2$. This scheme reduces patch-matching time by $\frac{2}{3}$ and improves robustness to noise by leveraging the cleaner green channel, facilitating group-level sparsity for collaborative filtering.

B. Global Circulant Representation

In the collaborative filtering step, the choice of algebraic representation plays a crucial role. In this section, we present an extension of the nonlocal circulant representation to a global formulation for patch modeling, enabling efficient capture of latent structures across different images.

1) *Nonlocal Circulant Formulation*: Following [28], by integrating the BCR into the nonlocal SVD problem and leveraging the notations of t-SVD and t-product, we can explore the patch-level correlation for each group via

$$\begin{aligned} & \min \sum_{i=1}^K \|\mathcal{P}_i - \mathcal{U} * \mathcal{S}_i * \mathcal{V}^T\|^2, \\ & \text{s.t. } \mathcal{U}^T \mathcal{U} = \mathcal{I}, \mathcal{V}^T \mathcal{V} = \mathcal{I}, \end{aligned} \quad (10)$$

where $\mathcal{S}_i \in \mathbb{R}^{ps \times ps \times 3}$ is the coefficient tensor, and $\mathcal{U}, \mathcal{V} \in \mathbb{R}^{ps \times ps \times 3}$ are orthogonal bases. This nonlocal t-SVD can be reduced to independent SVDs in the Fourier domain:

$$\begin{aligned} & \min \sum_{i=1}^K \|\widehat{\mathcal{P}}_i^{(j)} - \widehat{\mathcal{U}}^{(j)} \widehat{\mathcal{S}}_i^{(j)} \widehat{\mathcal{V}}^{(j)T}\|^2, \\ & \text{s.t. } \widehat{\mathcal{U}}^{(j)T} \widehat{\mathcal{U}}^{(j)} = \mathbf{I}, \widehat{\mathcal{V}}^{(j)T} \widehat{\mathcal{V}}^{(j)} = \mathbf{I}, \forall j \in 1, 2, 3, \end{aligned} \quad (11)$$

where $\widehat{\mathcal{P}}_i^{(j)}$ represents the j -th frontal slice of patch \mathcal{P}_i in the Fourier domain. The projection pairs $\widehat{\mathcal{U}}^{(j)}$ and $\widehat{\mathcal{V}}^{(j)}$ are given by the eigenvectors of the ensemble row-wise and column-wise correlation matrices $\mathbf{C}_{row} = \sum_{i=1}^K \widehat{\mathcal{P}}_i^{(j)} \widehat{\mathcal{P}}_i^{(j)T}$ and $\mathbf{C}_{col} = \sum_{i=1}^K \widehat{\mathcal{P}}_i^{(j)T} \widehat{\mathcal{P}}_i^{(j)}$, respectively.

2) *Global Patch-Level Projection*: It is noticed that if the observed patches are corrupted by additive white Gaussian noise (AWGN) $\mathbf{n} \sim N(0, \sigma^2)$, then for a large K

$$\sum_{i=1}^K \widehat{\mathcal{P}}_{noisy_i}^{(j)} \widehat{\mathcal{P}}_{noisy_i}^{(j)T} = \sum_{i=1}^K \widehat{\mathcal{P}}_{clean_i}^{(j)} \widehat{\mathcal{P}}_{clean_i}^{(j)T} + \sigma^2 \mathbf{I}. \quad (12)$$

This implies that the noise-free t-SVD bases of \mathcal{P}_{clean} can be approximated using numerous patches. To assess the effect of K , we apply a t-SVD denoiser [28] on real-world datasets (CC15 [39], HighISO [40], SIDD [41]). As shown in Fig. 3, performance gains become marginal for $K > 45$, indicating that excessively large groups are unnecessary.

However, learning separate bases for each group [28] introduces additional complexity. Since an image patch may share features with patches across the entire image, we consider to estimate a global projection pair \mathcal{U} and \mathcal{V} from all reference

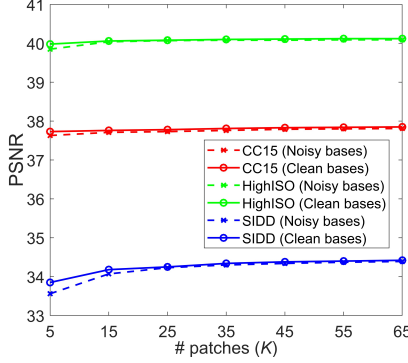


Fig. 3. Bases \mathcal{U} and \mathcal{V} learned from noisy and clean patches for varying K .

patches according to Equ. (11). We refer to this implementation as *globally-learned* t-SVD. Besides, it is interesting to investigate if the t-SVD bases acquired from a single image can be transferred to other images. Specifically, we utilize the first image from the CC15 dataset to learn a global pair of \mathcal{U} and \mathcal{V} , and then reuse them for all subsequent images. This variant is termed the *globally-reused* t-SVD. Fig. 4 illustrates different strategies for obtaining t-SVD bases \mathcal{U} and \mathcal{V} . As shown in Table I, the globally-reused approach achieves reliable estimation with reduced computational cost. This suggests that the learned bases can be directly applied to new observations while maintaining performance.

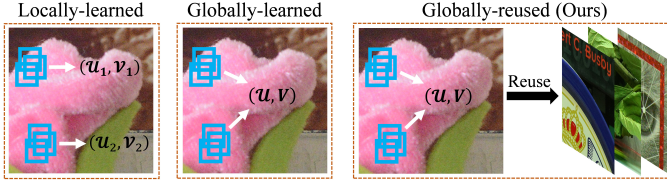


Fig. 4. Different strategies for obtaining t-SVD bases \mathcal{U} and \mathcal{V} .

TABLE I
PSNR/SSIM [42] COMPARISON OF t-SVD BASES \mathcal{U} AND \mathcal{V} OBTAINED WITH DIFFERENT STRATEGIES.

Dataset	Locally-learned	Globally-learned	Reused (Ours)	Clean
CC15	37.86/0.956	37.89/0.957	37.90/0.957	37.92/0.957
HighISO	40.05/0.968	40.13/0.969	40.15/0.970	40.19/0.970
SIDD-val	34.35/0.876	34.39/0.876	34.38/0.876	34.45/0.876
Time (s)	6.95	6.13	6.02	-

C. Local Circulant Structure

To further promote sparsity and suppress noise in the transform domain, exploiting group-level correlations among similar patches is essential. A common approach is to learn an invertible transform $\mathbf{U}_{group} \in \mathbb{R}^{K \times K}$ along the grouping dimension via PCA [28], [43], [44]. However, performing local PCA for each group incurs considerable computational cost. In this section, we present an alternative approach to bypass the explicit PCA learning.

1) *Group circulant formulation*: Due to limited search windows and noise contamination, only a small number of similar patches can usually be identified. To better exploit their correlations, we propose to extend the circulant structure to the stacked similar patches, enabling recursive modeling of

their interdependencies. Specifically, the circulant structure of a group \mathcal{G} containing K image patches can be defined as

$$circ(\mathcal{G}) = \begin{pmatrix} \mathbf{p}_1^T & \mathbf{p}_K^T & \cdots & \mathbf{p}_2^T \\ \mathbf{p}_2^T & \mathbf{p}_1^T & \cdots & \mathbf{p}_{K-1}^T \\ \vdots & \vdots & \ddots & \vdots \\ \mathbf{p}_K^T & \mathbf{p}_{K-1}^T & \cdots & \mathbf{p}_1^T \end{pmatrix} \in \mathbb{R}^{K \times 3Kps^2}, \quad (13)$$

where $\mathbf{p}_i \in \mathbb{R}^{3ps^2 \times 1}$ is the vector form of the i -th patch \mathbf{p}_i of \mathcal{G} . This construction replicates each patch across all rows, thereby explicitly encoding group-level redundancy. To efficiently exploit such correlations without explicit learning on the large matrix $circ(\mathcal{G})$, we examine its structural property. Let \mathbf{r}_i^T denotes the i -th row of $circ(\mathcal{G})$, then

$$\mathbf{r}_i^T = [\mathbf{p}_{(j+i-2 \bmod K)+1}^T]_{j=1}^K, \quad \forall i = 1, 2, \dots, K. \quad (14)$$

From Equ. (13) and Equ. (14), we notice that each row is a cyclic permutation of K patches, thus the Gram matrix $circ(\mathcal{G})circ(\mathcal{G})^T \in \mathbb{R}^{K \times K}$ preserves the circulant structure:

$$circ(\mathcal{G})circ(\mathcal{G})^T = \begin{pmatrix} \mathbf{r}_1^T \mathbf{r}_1 & \mathbf{r}_1^T \mathbf{r}_2 & \cdots & \mathbf{r}_1^T \mathbf{r}_K \\ \mathbf{r}_2^T \mathbf{r}_1 & \mathbf{r}_2^T \mathbf{r}_2 & \cdots & \mathbf{r}_2^T \mathbf{r}_K \\ \vdots & \vdots & \ddots & \vdots \\ \mathbf{r}_K^T \mathbf{r}_1 & \mathbf{r}_K^T \mathbf{r}_2 & \cdots & \mathbf{r}_K^T \mathbf{r}_K \end{pmatrix}. \quad (15)$$

2) *Relationship to PCA and the Haar Transform*: The EVD of the matrix in Equ. (15) is given by

$$circ(\mathcal{G})circ(\mathcal{G})^T \mathbf{u} = \lambda \mathbf{u}, \quad (16)$$

where λ and $\mathbf{u} \in \mathbb{R}^K$ denote an eigenvalue and its corresponding eigenvector, respectively. An interesting observation of the circulant pattern $circ(\mathcal{G})$ from Equ. (13) and Equ. (14) is that the sum of each row and column of $circ(\mathcal{G})$ is identical. Denoting this common row sum by \mathbf{r}_{sum}^T , we have

$$\mathbf{r}_{sum}^T = \sum_{i=1}^K \mathbf{p}_i^T. \quad (17)$$

Leveraging the circulant property of both $circ(\mathcal{G})$ and its Gram matrix in Equ. (15), the dominant eigenpair $(\lambda_{max}, \mathbf{u}_{max})$ of $circ(\mathcal{G})circ(\mathcal{G})^T$ can be obtained by

$$\begin{aligned} \lambda_{max} &= \sum_{i=1}^K \mathbf{p}_i^T \sum_{i=1}^K \mathbf{p}_i = \mathbf{r}_{sum}^T \mathbf{r}_{sum}, \\ \mathbf{u}_{max} &= \frac{1}{\sqrt{K}} (1, 1, \dots, 1)^T. \end{aligned} \quad (18)$$

Interestingly, when K is a power of 2, the dominant eigenvector \mathbf{u}_{max}^T coincides with the first row of the Haar transform matrix defined in Equ. (8). This reveals that the Haar transform inherently encodes the first principal component of $circ(\mathcal{G})circ(\mathcal{G})^T$. Since noise can be suppressed by discarding small coefficients in the transform domain, the orthogonal Haar bases provide an efficient data-agnostic alternative to PCA under circulant formulation. Accordingly, the group-level transform can be modeled by the Haar transform.

Employing the Haar transform enjoys two computational benefits. First, it enables modeling the group-level redundancy without explicitly constructing the circulant matrix. Second, the predefined Haar matrix \mathbf{U}_{Haar} eliminates the need to obtain a distinct \mathbf{U}_{group} for each group \mathcal{G}_{noisy} .

D. The Haar-tSVD Transform

1) *One-step Filtering*: The above analysis of the circulant representation allows us to get rid of local transform learning. By combining the patch-level projection pair $(\mathcal{U}, \mathcal{V})$ with the group-level Haar matrix $\mathbf{U}_{\text{group}}$, we obtain a plug-and-play transform. As a result, the proposed Haar-tSVD method admits a simple one-step collaborative filtering scheme, as summarized in Algorithm 1. Specifically, the coefficients $\mathcal{S}_{\text{noisy}}$ can be derived by performing the forward transform $\mathcal{T}_{\text{forward}}$ via

$$\mathcal{S}_{\text{noisy}} = \mathcal{U}^T * \mathcal{G}_{\text{noisy}} * \mathcal{V} \times_4 \mathbf{U}_{\text{Haar}}. \quad (19)$$

Hard-thresholding $\mathcal{T}_{\text{threshold}}$ [45] is then applied to shrink the coefficients of $\mathcal{S}_{\text{noisy}}$ under threshold τ via

$$\mathcal{S}_{\text{truncate}} = \begin{cases} \mathcal{S}_{\text{noisy}}, & |\mathcal{S}_{\text{noisy}}| \geq \tau, \\ 0, & |\mathcal{S}_{\text{noisy}}| < \tau. \end{cases} \quad (20)$$

The estimated clean group $\mathcal{G}_{\text{estimate}}$ is recovered by taking the inverse $\mathcal{T}_{\text{inverse}}$ of Equ. (19) with $\mathcal{S}_{\text{truncate}}$:

$$\mathcal{G}_{\text{estimate}} = \mathcal{U} * \mathcal{S}_{\text{truncate}} * \mathcal{V}^T \times_4 \mathbf{U}_{\text{Haar}}^{-1}. \quad (21)$$

Finally, the denoised patches in $\mathcal{G}_{\text{estimate}}$ are aggregated back to their original image locations.

Algorithm 1 Haar-tSVD

Input: Noisy image \mathcal{Y} , patch size ps , number of similar patches K , search window size W , and noise level σ .

Output: Estimated clean image \mathcal{X} .

- 1: **for** each reference patch \mathcal{P}_{ref} **do**
- 2: **Grouping:** Search K most similar patches within window W using Equ. (9) to form group $\mathcal{G}_{\text{noisy}}$.
- 3: **Filtering:** Apply the forward-threshold-inverse transform in Equs. (19)–(21) for the estimated group via $\mathcal{G}_{\text{estimate}} = \mathcal{T}_{\text{inverse}} \circ \mathcal{T}_{\text{threshold}} \circ \mathcal{T}_{\text{forward}}(\mathcal{G}_{\text{noisy}})$.
- 4: **Aggregation:** Averagely write all patches of $\mathcal{G}_{\text{estimate}}$ back to their original locations.
- 5: **end for**

2) *Complexity analysis*: The computational cost of the proposed Haar-tSVD for each local group consists of three parts: (i) the search of K similar patches within a window $O(KW^2ps)$, (ii) the global t-SVD projection $O(Kps^3)$, and (iii) the Haar transform projection $O(K^3)$. By adopting the fast Haar transform [36], the group-level projection can be reduced to $O(K \log K)$. Therefore, an overall computational complexity of Haar-tSVD is $O([KW^2ps + Kps^3 + K \log K])$. Compared to many effective t-SVD based approaches [22], [28], [38], [46], [47], the proposed method is more efficient, because it does not involve any local learning procedure.

3) *Fast implementation*: The proposed method consists of two major components: patch-matching and global-local transform, both of which are inherently parallelizable. Specifically, patch-matching involves only Euclidean distance computations, while the transform bases \mathcal{U} , \mathcal{V} and \mathbf{U}_{Haar} are shared by all patch groups. Therefore, the computation is dominated by matrix–vector multiplications, making the method suitable for parallel implementation. We achieve over $10\times$ speedup compared to the baseline MATLAB serial implementation. In

practice, further acceleration can be obtained by caching intermediate results such as patch indices and transform coefficients $\mathcal{S}_{\text{noisy}}$ during parameter selection.

E. Adaptive Scheme and Enhancement Strategy

1) *Adaptive noise estimation*: Apart from an effective collaborative filtering scheme, noise estimation is crucial for an efficient denoiser. For Haar-tSVD, the noise level σ characterizes the sparsity of coefficients in the transform domain. To model the sparsity level, we can reformulate the noise estimation problem as a classification task and train a noise estimator using CNN [38], as illustrated in Fig. 5.

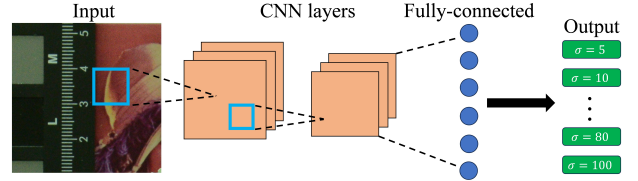


Fig. 5. The CNN-based noise estimation approach.

However, we notice that the rationale for incorporating a DNN-based noise estimator also hinges on the robustness of local adaptive transform to small perturbations in σ . The prediction accuracy of the CNN estimator on real-world data reported in Table II indicates limited generalization results. Misclassification of the noise level σ can degrade the performance of Haar-tSVD. As shown in Fig. 6, although Haar-tSVD achieves denoising quality comparable to PCA-tSVD [38], its fixed bases are more sensitive to noise-level variations, potentially leading to oversmoothing effects.

TABLE II
AVERAGE PREDICTION ACCURACY OF THE CNN-BASED ESTIMATOR ON REAL-WORLD DATASETS.

Dataset	CC15	HighISO	SIDD-validation
Accuracy (%)	69.3	71.2	75.1

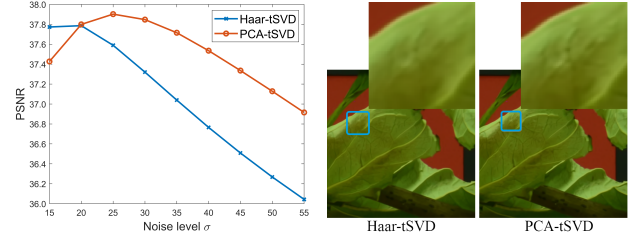


Fig. 6. Denoising effects of the Haar and PCA transforms for $\mathbf{U}_{\text{group}}$.

To enhance adaptiveness, we further analyze the eigenvalue characteristics of the circulant matrix $\text{circ}(\mathcal{G})\text{circ}(\mathcal{G})^T$. Due to its circulant structure, an eigenpair $(\hat{\lambda}, \hat{\mathbf{u}})$ is given by

$$\begin{aligned} \hat{\lambda} &= \sum_{i=1}^K (-1)^i \mathbf{p}_i^T \sum_{i=1}^K (-1)^i \mathbf{p}_i, \\ \hat{\mathbf{u}} &= \frac{1}{\sqrt{K}} (-1, 1, \dots, -1, 1)^T. \end{aligned} \quad (22)$$

Equ. (22) indicates that the eigenpair captures the alternating contrast between adjacent patches within a local group

\mathcal{G} . Therefore, we can use $\hat{\lambda}$ to measure the inner-group similarity. Specifically, in low-noise conditions, high inner-group similarity yields small $\hat{\lambda}$, whereas severe noise disrupts patch-matching and shifts $\hat{\lambda}$ toward larger eigenvalues. To demonstrate the impact of noise, we denote by a the rank position of $\hat{\lambda}$ among the K eigenvalues sorted in ascending order. As illustrated in Fig. 7, for $K = 32$, a increases significantly with noise severity, suggesting that a can serve as an indicator of noise strength.

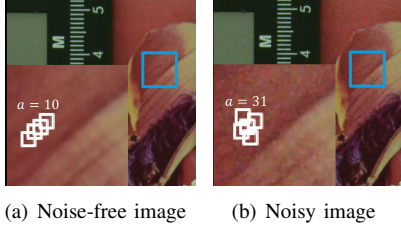


Fig. 7. Influence of real-world noise on patch-search and rank position a .

Accordingly, the CNN-estimated noise level σ_{est} is adaptively adjusted as

$$\hat{\sigma} = \begin{cases} \frac{1}{\beta} \sigma_{est}, & a \leq \gamma, \\ \sigma_{est}, & a > \gamma, \end{cases} \quad (23)$$

where $\hat{\sigma}$ is the final estimated noise level, β and γ are weighting parameters empirically set to 1.2 and 13, respectively. From Equ. (23), we notice that it is unnecessary to perform full EVD to determine a . To further reduce computational complexity, we avoid adjusting σ_{est} for every local group \mathcal{G} . Instead, we randomly sample a few groups within a subimage and obtain the corresponding $\hat{\sigma}$ through majority voting.

We term the proposed method with the adaptive noise estimation strategy as *A-Haar-tSVD*. As illustrated in Fig. 8, the adaptive approach incorporates the effectiveness of CNNs, preserves the simplicity of patch-based framework and leverages the adaptability of eigenvalue analysis.

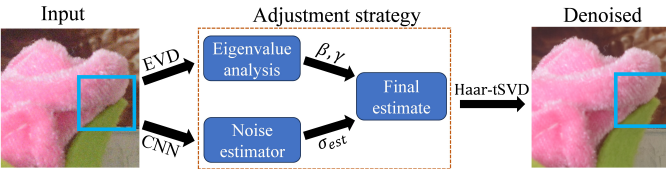


Fig. 8. Flowchart of the adaptive variant A-Haar-tSVD.

2) *Enhancement under severe noise*: Classic patch-based denoisers are particularly subject to severe noise [1], [10], which degrades patch-matching accuracy and contaminates transform-domain coefficients. As illustrated in Fig. 9, both the proposed Haar-tSVD and the state-of-the-art BM3D exhibit noticeable color artifacts, even when the noise level is properly estimated. To further improve robustness of the proposed method under severe noise, we present an enhancement strategy, termed *RA-Haar-tSVD*, which integrates a lightweight, trainable refinement module into the Haar-tSVD framework. Fig. 9 shows its effectiveness to remove artifacts and restore natural color in the challenging high-noise scenario.

According to the Haar-PCA link in Equ. (18), the first

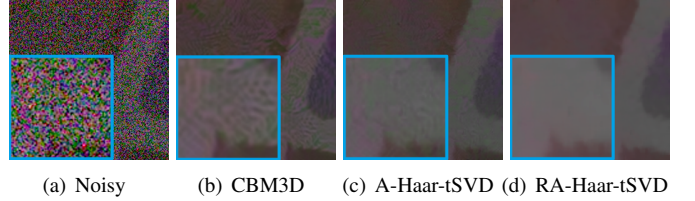


Fig. 9. Effects of the robust enhancement strategy under severe noise. row of the Haar matrix corresponds to the dominant eigenvector \mathbf{u}_{max} and captures the weighted mean of all patches $\mathbf{p}_{noisy} \in \mathbb{R}^{K \times 1}$ of a group \mathcal{G}_{noisy} in the transform domain:

$$\mathcal{G}_{noisy} \times 4 \mathbf{u}_{max}^T = \frac{1}{\sqrt{K}} \sum_{i=1}^K \mathbf{p}_{noisy_i} = \sqrt{K} \cdot \bar{\mathbf{p}}_{noisy}, \quad (24)$$

where the weighted mean patch $\sqrt{K} \cdot \bar{\mathbf{p}}_{noisy}$ is the first row of the group-level projection $\mathcal{G}_{noisy} \times 4 \mathbf{U}_{Haar}$ and preserves most of its signal energy. However, \mathbf{p}_{noisy} is severely contaminated due to the rare-patch effect, which propagates visible artifacts to the reconstructed image. To address this issue, we employ a plain fully connected network (FCN) [48] to obtain a cleaner version of the dominant coefficients $\bar{\mathbf{p}}_{est}$ via

$$\bar{\mathbf{p}}_{est} = FCN_{\theta}(\bar{\mathbf{p}}_{noisy}). \quad (25)$$

As illustrated in Fig. 10, the estimated mean patch $\bar{\mathbf{p}}_{est}$ of the FCN is used to refine the first row of the group-level projection \mathbf{G}_{Haar} . This strategy offers three advantages: (i) it utilizes the feature extraction ability of the network to obtain the dominant group component under severe noise; (ii) abundant noisy-clean pairs of mean patches are available from overlapping groups for training; and (iii) only the dominant Haar coefficients are modified, the remaining components are preserved and local structural information is retained.

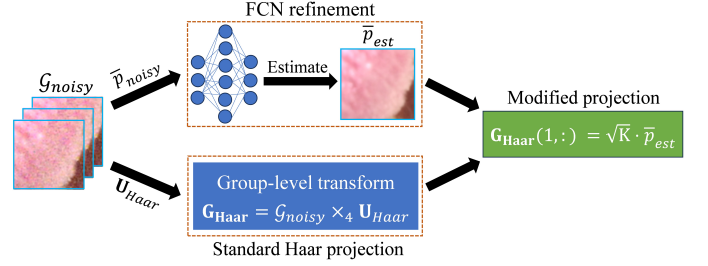


Fig. 10. Flowchart of the RA-Haar-tSVD enhancement strategy for a group.

F. Related Patch-based Denoisers

Table III compares the proposed Haar-tSVD and its variants with representative patch-based denoisers in terms of learning strategy and implementation. Built upon the t-SVD and Haar transforms, the proposed method absorbs the ideas from the simple and effective design of classic denoisers. Instead of recursively solving complex optimization problems, the proposed Haar-tSVD aims at one-step filtering that eliminates the need to train local bases for each image. Under circulant representation, we employ a unified global t-SVD and Haar transform to efficiently capture patch- and group-level correlation. Besides, EVD is leveraged for adaptive noise estimation, and the integration of NNs with the Haar-tSVD provides an extra enhancement mechanism under severe noise.

TABLE III
REPRESENTATIVE TRADITIONAL DENOISERS WITH DIFFERENT ALGEBRAIC REPRESENTATIONS AND ENHANCEMENT STRATEGIES.

Category	Algebra	Methods	Parallel impl.	Global transform	One-step filter	Adaptive scheme	Enhancement	Key words
Patch-based denoisers	Matrix	DCT [49]	✓	✓	✓	-	-	Discrete cosine transform filter
		NLPCA [43]	✓	-	-	-	✓	Nonlocal PCA
		MCWNMM [50]	-	-	-	-	✓	Weighted nuclear norm
		TWSC [18]	-	-	-	✓	✓	Trilateral sparse coding
		GID [51]	-	-	-	✓	✓	External + internal prior
		NLH [35]	✓	✓	-	-	✓	Haar-based NLM
		Bitonic [52]	✓	-	-	✓	✓	Bitonic filtering
Patch-based denoisers	Tensor	BM4D [53]	✓	✓	-	-	✓	4D extension of BM3D
		HOSVD [54]	-	✓	✓	-	✓	4D HOSVD transform
		TDL [55]	-	-	-	-	✓	Tucker dictionary learning
		LLRT [56]	-	-	-	✓	✓	LR tensor + Laplacian
		MSt-SVD [28]	✓	-	✓	-	-	One-step t-SVD
		LTDL [46]	-	-	-	-	✓	LR tensor dictionary learning
		GCP-ID [38]	✓	-	✓	✓	-	Green channel prior + t-SVD
		Haar-tSVD (Ours)	✓	✓	✓	-	-	Global-local circulant structure
		A-Haar-tSVD (Ours)	✓	✓	✓	✓	-	Adaptive noise estimation
		RA-Haar-tSVD (Ours)	✓	✓	✓	✓	✓	Adaptive noise estimation

IV. EXPERIMENTS

In this section, we evaluate about 50 denoising methods across images, video, and HSI datasets. For each method, original implementations or published results are used, with parameters/models carefully chosen for optimal performance. GPU-accelerated methods are executed using the computational resources of Google Colab Pro, while all remaining experiments are conducted on a workstation equipped with an Intel Core i7-10700F CPU @ 2.9 GHz and 16 GB RAM. More details are provided in the supplementary material.

A. Implementation Details

Haar-tSVD. It involves four primary parameters: the patch size ps , the number of similar patches K within a group, the window size W for patch search, and the hard-thresholding parameter τ . For image, video and HSI data, we set $ps = 8$, $K = 32$, $W < 20$ and $\tau = \sigma \sqrt{2 \log(cKps^2)}$, where c denotes the number of channels or spectral bands.

A-Haar-tSVD and RA-Haar-tSVD. A multi-layer CNN [57] and a FCN are adopted for noise level prediction and mean-patch estimation, respectively. The SIDD small and CC60 [51] data are used for training. For A-Haar-tSVD, each input is divided into subimages of size 128×128 , and the noise level σ is selected from $\{1.25, 5, 10, 20, 30, 40, 50, 60, 80, 100, 120\}$. For RA-Haar-tSVD, each input \bar{P}_{noisy} is the mean patch of a local group, and the network is trained using residual-learning.

B. Color Image Denoising

We perform synthetic and real-world experiments. For synthetic denoising, we use the Kodak dataset [58] and add independent noise to each RGB to simulate channel-specific corruption. In *case 1*, the noise variances are $[15, 10, 20]$, and in *case 2*, they are $[40, 30, 50]$. For Gaussian denoisers, the noise levels σ are set to 20 and 50, respectively.

1) *Objective results:* Table IV evaluates the results of traditional patch-based denoisers and supervised/self-supervised DNN models. Overall, Haar-tSVD achieves competitive performance, its adaptive variant A-Haar-tSVD improves results across datasets, and the enhancement strategy RA-Haar-tSVD further boosts performance under severe noise. On the Kodak dataset, we notice that RA-Haar-tSVD is particularly beneficial when the noise level is high, whereas at lower noise

levels, NN-based estimation may suffer from oversmoothness. Therefore, on real-world datasets, we apply the enhancement scheme when $\sigma > 30$. Beyond Kodak, A-Haar-tSVD achieves PSNR gains of at least 0.24dB and 0.84dB over CBM3D and MSt-SVD on DND and SIDD, respectively, while RA-Haar-tSVD shows additional improvements in challenging scenarios. On CC, PolyU, HighISO, and IOCI, the proposed methods demonstrate their adaptiveness and generalization compared with many DNN models that degrade when training or validation data are not available.

Ideally, the enhancement strategy should be applied only when necessary. To better understand its potential, Table V assesses its effects in cases where measurable gains are observed. Under this ideal setting, RA-Haar-tSVD consistently outperforms the adaptive baseline, with obvious advantages under severe noise, demonstrating its potential in handling different degradations.

TABLE V
EVALUATION OF RA-HAAR-TSVD UNDER IDEAL SETTINGS.

Method	DND	SIDD	CC15	PolyU	HighISO	IOCI
A-Haar-tSVD	38.25	35.58	38.24	38.89	40.62	41.52
RA-Haar-tSVD (ideal)	38.64	37.48	38.56	38.95	40.68	41.60
Improvement	0.39	1.90	0.32	0.06	0.06	0.08

2) *Visual evaluations:* Visual evaluations are presented in Fig. 11 to Fig. 13. Specifically, Fig. 11 shows the effectiveness of integrating NNs with circulant representation for noise removal and detail preservation, while compared methods slightly over-smooth textures in certain regions. Fig. 12 highlights the limitations of patch-based denoisers when handling heavily corrupted images, where noise disrupts grouping and local transforms. Nevertheless, the proposed method produces less distortions and color artifacts compared to SASL and Bitonic, thanks to the redundancy encoded in the global-local circulant structures and the enhancement strategy. Fig. 13 shows that when confronted with unseen noise patterns, the well-trained DNN models may leave unwanted artifacts and suffer from over-smooth effects. By comparison, the adaptive scheme shows its strengths by exploiting both the CNN estimator and nonlocal information, which render certain robustness and adaptability, therefore achieving a balance between noise suppression and detail recovery.

TABLE IV
DENOISING COMPARISON ON REAL-WORLD SRGB COLOR IMAGE DATASETS. ‘*’: THE RESULTS ARE FROM THE AUTHORS’ PAPERS.

Methods/Models	Kodak (case 1)	Kodak (case 2)	DND [59]	SIDD [41]	CC15 [39]	PolyU [60]	HighISO [40]	IOCI [10]
Traditional denoisers	Bitonic [52]	-	-	37.85/0.936	36.67/0.933	35.22/0.924	36.64/0.939	37.37/0.943
	MCWNNM [50]	28.40/0.792	26.54/0.686	37.38/0.929	29.54/0.888	37.02/0.950	38.26/0.965	39.89/0.970
	NLHCC [35]	-	-	38.85/0.953	35.31/0.930	38.49/0.965	38.36/0.965	40.29/0.971
	MSt-SVD [28]	33.99/0.906	29.12/0.770	38.01/0.938	34.38/0.901	37.95/0.959	38.85/0.971	40.49/0.974
	CBM3D [61]	33.51/0.893	28.90/0.780	37.73/0.934	34.74/0.922	37.70/0.957	38.69/0.970	40.35/0.974
Traditional + DNN	Haar-tSVD (ours)	34.13/0.910	29.16/0.780	38.11/0.939	35.05/0.914	38.10/0.961	38.78/0.969	40.51/0.973
	A-Haar-tSVD (ours)	34.04/0.907	29.18/0.783	38.25/0.944	35.58/0.925	38.24/0.963	38.89/0.971	40.62/0.974
	RA-Haar-tSVD (ours)	33.89/0.901	29.19/0.787	38.64/0.945	37.48/-	38.30/0.962	38.85/0.970	40.63/0.975
DNN models (Self-supervised)	Pixel2Pixel [62]	30.26/0.841	26.88/0.718	-	34.34*/-	35.51/0.923	37.19/0.951	37.77/0.945
	APR-RD [63]	26.12/0.713	23.21/0.634	38.57/0.942	38.23*/-	35.83/0.946	37.01/0.953	38.75/0.968
	B2UB [64]	29.91/0.816	26.80/0.698	-	-	36.51/0.935	38.25/0.968	39.03/0.962
	Noise2VST [65]	34.08/0.907	28.34/0.771	-	-	33.96/0.868	36.60/0.929	35.99/0.893
	SASL [66]	26.52/0.728	23.69/0.638	38.01/0.936	-	34.93/0.936	37.13/0.954	38.24/0.964
DNN models (Supervised)	TBSN [67]	27.47/0.745	24.63/0.662	37.79/0.940	39.01/0.945	35.73/0.931	36.51/0.954	38.84/0.966
	Zero-shot [68]	-	-	-	35.05/0.922	37.20/0.948	37.88/0.959	-
	ClipDe [69]	30.94/0.871	20.97/0.618	39.57/0.954	39.42/0.956	35.40/0.915	36.87/0.939	37.61/0.954
	Condformer [70]	-	-	40.10/0.956*	40.23*/-	36.34/0.922	37.27/0.947	37.79/0.927
	DeepSN [71]	-	-	39.92/0.956	39.79/0.958	35.89/0.936	37.25/0.956	38.12/0.950
DNN models (Supervised)	DIDN [72]	27.68/0.802	21.85/0.654	39.64/0.953	39.78/0.958	36.06/0.946	37.36/0.953	38.24/0.950
	DMID [73]	-	-	-	-	37.09*/-	37.59/0.946	37.90/0.931
	FFDNet [74]	33.57/0.891	28.94/0.765	37.61/0.942	38.27/0.948	37.67/0.956	38.76/0.970	40.28/0.973
	IDF [75]	31.88/0.851	27.96/0.764	33.72/0.811	-	36.43/0.942	37.77/0.962	38.63/0.960
	MaIR [76]	32.86/0.873	28.61/0.781	-	39.92/0.959	36.05/0.938	37.64/0.958	38.38/0.953
DNN models (Supervised)	NAFNet [7]	-	-	38.36/0.943	40.15/0.960	34.39/0.923	36.38/0.947	37.88/0.954
	Restormer [8]	31.51/0.845	27.31/0.745	40.03/0.956	40.02/0.960	36.33/0.941	37.66/0.956	38.29/0.948

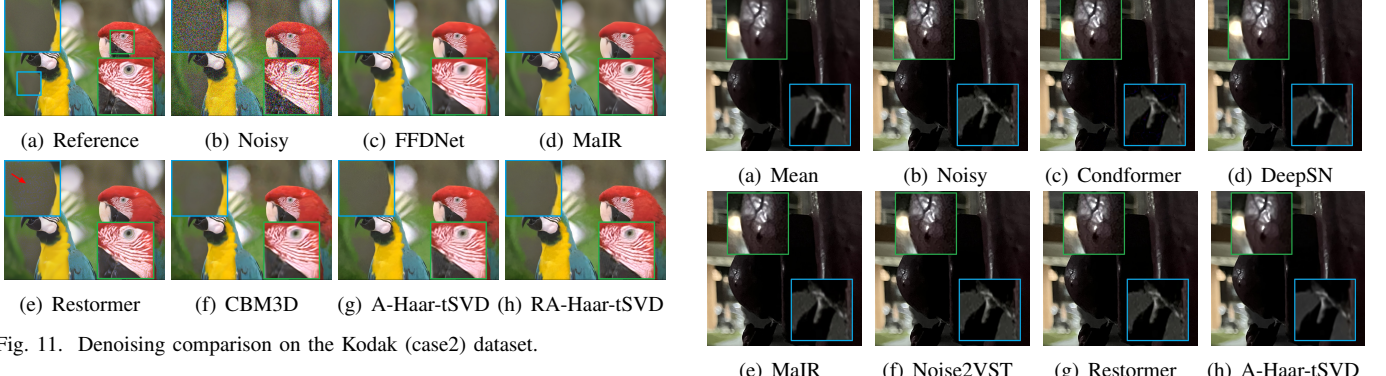


Fig. 11. Denoising comparison on the Kodak (case2) dataset.

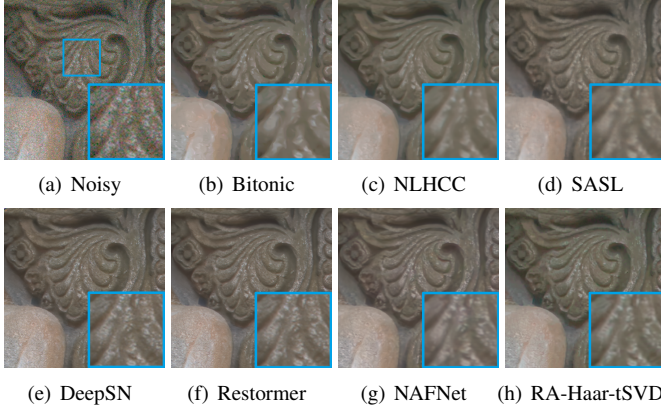


Fig. 12. Denoising comparison on the DND dataset.

3) *Denoising efficiency*: As reported in Table VI, supervised DNN models benefit from modern GPUs and achieve fast inference. For example, Restormer and Condformer can process an image of size $512 \times 512 \times 3$ within 1 second. The proposed Haar-tSVD is among the few methods parallel with the state-of-the-art BM3D in terms of both efficiency

Fig. 13. Denoising comparison on the IOCI dataset.

and effectiveness, as its grouping is performed only on the green/opponent channel and it avoids recursive learning of local transforms. Moreover, compared with other complex network architectures, RA-Haar-tSVD is lightweight and enjoys considerably low complexity. In particular, the simple CNN noise estimator and the FCN used in the adaptive and enhancement strategies require less than $\frac{1}{50}$ of the training time of an advanced model like Restormer. This combination of channel-wise prior, lightweight design, and avoidance of repeated local learning makes the proposed method highly practical for real-world denoising applications.

TABLE VI
COMPUTATIONAL COMPLEXITY OF DIFFERENT DENOISING METHODS
WHEN PROCESSING $512 \times 512 \times 3$ SRGB IMAGES.

Method	CBM3D	NLHCC	RA-Haar-tSVD	DIDN	Condformer	Restormer
Test time (s)	3.6	41.2	4.5	7.3	0.9	0.8
Train time (m)	-	-	23.2	-	-	> 1000
# Params (M)	-	-	7.5	22.1	26.4	25.3

TABLE VII
QUANTITATIVE COMPARISON ON REAL-WORLD COLOR VIDEO DENOISING DATASETS. BEST RESULTS ARE HIGHLIGHTED IN BOLD.

Dataset	Traditional denoisers				Traditional + DNN				DNN models					
	MSt-SVD [28]	VBM4D [77]	VIDOSAT [78]	Haar-tSVD (Ours)	A-Haar-tSVD (Ours)	RA-Haar-tSVD (Ours)	VNLNet [79]	DVDNet [80]	FastDVDNet [81]	FloRNN [82]	STBN [83]	UDVD [84]	ViDeNN [85]	VRT [86]
CRVD [87]	36.66 0.946	34.14 0.908	34.16 0.938	36.80 0.953	37.00 0.961	37.13 0.963	36.11 0.945	34.50 0.949	35.84 0.931	36.66 0.960	36.51 0.960	- -	32.31 0.845	36.94 0.956
IOCV [10]	38.22 0.974	38.76 0.976	- -	38.83 0.976	38.92 0.977	39.04 0.978	38.76 0.977	38.53 0.975	37.57 0.970	38.64 0.974	38.76 0.977	35.02 0.966	36.13 0.951	38.50 0.967

C. Real-world Color Video Denoising

Videos are more informative than images with dynamic objects and temporal continuity. The proposed method can be readily extended to handle video sequences. Specifically, for Haar-tSVD, the patch search is applied to both spatial and temporal dimension. The trained CNN-based estimator and the adaptive noise adjustment of A-Haar-tSVD can be adopted in a frame-by-frame fashion, while the enhancement strategy is imposed on groups obtained from spatio-temporal patch search. In our experiments, all video sequences of CRVD and IOCV are used for evaluations. The objective metrics are computed as the average across all frames [81]. Table VII lists the quantitative results of compared methods. The proposed method achieves very competitive results on both datasets, and the enhancement strategy RA-Haar-tSVD outperforms baselines by a margin of at least 0.28dB in PSNR. These results demonstrate the effectiveness of combining the global t-SVD with the Haar transform in capturing the nonlocal characteristics of video data across frames.

Visual comparisons are provided in Fig. 14 to Fig. 16. As shown in Fig. 14 and Fig. 15, even under moderate noise levels, the pretrained DNN models tend to exhibit more obvious over-smooth effects. In particular, Fig. 15 depicts a scene with static background, where the toy girl in blue is dynamic and moves in more than one directions. Consequently, some details and textures appear only in certain frames. Benefiting from the adaptive noise estimation strategy and the nonlocal characteristics, the proposed A-Haar-tSVD method effectively captures spatiotemporal similarity and preserves more structural information. Besides, Fig. 16 demonstrates the robustness of the proposed enhancement strategy to severe noise corruptions. By leveraging the patch- and group-level redundancy across different frames, the proposed method is able to suppress noise and mitigate color artifacts.

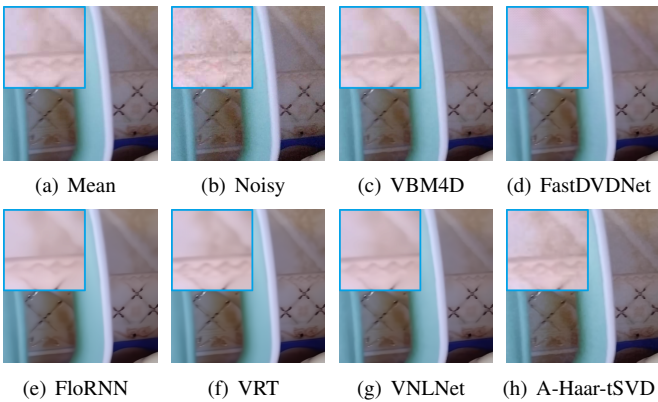


Fig. 14. Denoising comparison on the IOCV dataset.

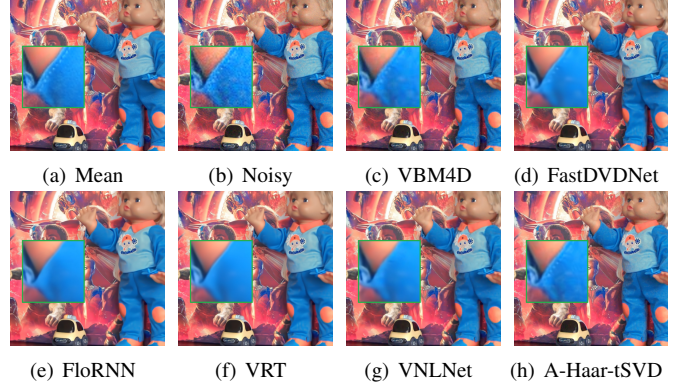


Fig. 15. Denoising comparison on the CRVD dataset (ISO = 6400).

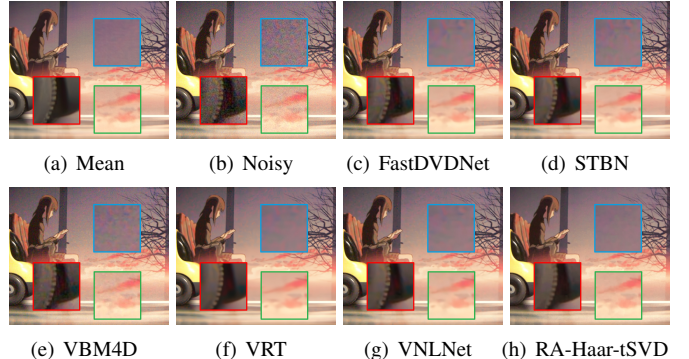


Fig. 16. Denoising comparison on the CRVD dataset (ISO = 12800).

D. Real-world HSI Denoising

HSI plays a vital role in a variety of remote sensing applications [98]. To handle an HSI data $\mathcal{Y} \in \mathbb{R}^{H \times W \times N_{\text{bands}}}$, we treat each local patch as a long tube and set $ps = 8 \times 8 \times N_{\text{bands}}$, while other parameters are kept the same as those used in the image denoising task. To apply the CNN noise estimator without retraining, we estimate the noise of \mathcal{Y} based on the mean value across all spectral bands. Objective results of compared methods are given in Table VIII. By effectively capturing the rich spatial-spectral correlations in HSI data with circulant structures, the proposed Haar-tSVD and its adaptive variant achieve competitive performance compared with state-of-the-art approaches. Meanwhile, by eliminating the need for complex iterative filtering and local transform learning, our method attains inference time comparable to advanced DNN models. These properties make it a practical and efficient solution for large-scale HSI denoising.

Visual comparisons of competitive methods on the Real-HSI dataset are shown in Fig. 17. We can see that The proposed method achieves a good balance between smoothness and detail preservation. In contrast, BM4D tends to produce

TABLE VIII
DENOISING RESULTS OF COMPARED METHODS ON THE REAL-HSI DATASET.

Datasets	Metrics	Traditional denoisers							DNN methods						
		BM4D [53]	LLRT [56]	LTDL [46]	MS+SVd [28]	NGMeet [88]	SSTPTV [89]	Haar-tSVD (Ours)	A-Haar-tSVD (Ours)	FlexDID [90]	HSI-DeNet [91]	Mac-Net [92]	QRNN3D [93]	RAS2S [94]	sDeCNN [95]
Real-HSI	PSNR \uparrow	25.88	25.90	25.80	25.86	25.87	25.21	25.82	25.81	25.31	25.63	25.88	25.82	25.87	25.70
	SSIM \uparrow	0.865	0.861	0.841	0.866	0.866	0.815	0.865	0.866	0.820	0.853	0.863	0.869	0.868	0.860
	SAM [96] \downarrow	0.066	0.060	0.074	0.063	0.051	0.072	0.063	0.064	0.075	0.092	0.056	0.064	0.054	0.093
	EGRAS [97] \downarrow	222.68	224.05	223.32	222.64	222.69	233.51	222.96	223.12	232.12	232.73	222.84	225.32	222.83	227.88
Platform	-	CPU	CPU	CPU	CPU	CPU	CPU	CPU	CPU/GPU	GPU (T4)	GPU (T4)	GPU (T4)	GPU (T4)	GPU (T4)	GPU (T4)
Time	minutes	4.1	16.5	35.0	2.8	4.1	4.9	0.1	0.2	6.1	0.8	0.2	0.1	0.1	0.7

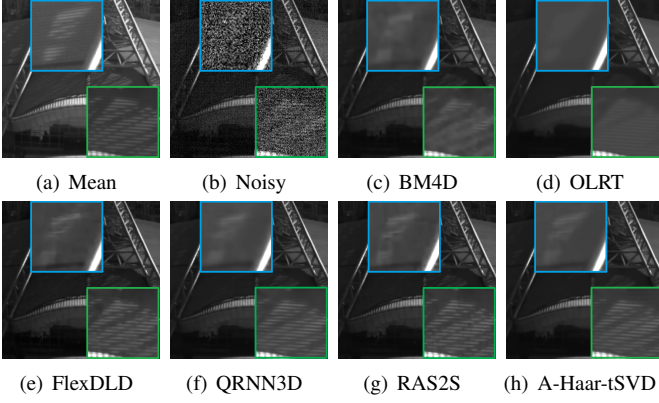


Fig. 17. Denoising comparison on the Real-HSI dataset.

obvious oversmooth effects, since its predefined patch-level transforms may not fully exploit the correlation across all the spectral bands. Additionally, the state-of-the-art low-rank tensor method OLRT struggles to preserve high-frequency components such as edges and textures. These observations suggest that increasing the number of iterations and similar patches may not help preserve fine details and structure of HSI data. Moreover, although the DNN-based methods FlexDLD and RAS2S demonstrate impressive noise suppression, they introduce mild artifacts. Fig. 18 illustrates the spectral reflectance curves of the ground-truth and the reconstructed HSIs, further confirming the competitive performance of our method in this challenging scenario.

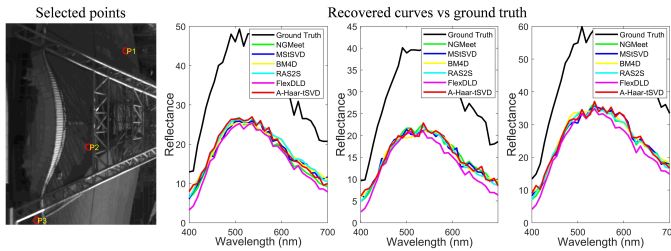


Fig. 18. Spectral curves of randomly selected points across different regions.

In many cases, the noise distribution can be highly non-uniform across spectral bands, with a few bands suffering from severe contamination. To address this issue, we perform band-wise noise estimation, enabling the identification of heavily corrupted bands based on the predicted noise level σ_{est} , as illustrated in Fig. 19. For severely contaminated bands (defined as $\sigma_{est} > 2\sigma_{mean}$, where σ_{mean} denotes the mean noise level across all bands), we adopt the highest noise estimation output to ensure noise suppression. The idea is to exploit the rich redundancy information inherent in HSI tubes to achieve noise

removal. However, this may cause oversmooth effects to the cleaner bands. Therefore, for the less corrupted spectral bands, we can refine the denoising result by adopting their mean noise estimation value σ_{mean} to preserve fine details.

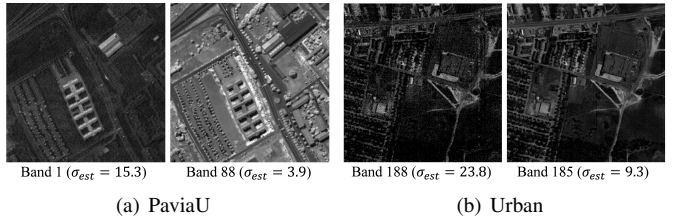


Fig. 19. Estimated noise σ_{est} for different bands with the proposed strategy.

Visual evaluations for several real-world HSI datasets are provided in Fig. 20 to Fig. 22, illustrating the proposed method's performance on challenging cases. The qualitative evaluations suggest that benefiting from the adaptive noise estimation scheme, the proposed method can achieve promising results. In particular, Fig. 21 and Fig. 22 demonstrate its ability of handling complex noise patterns, showing a reasonable ability to suppress both random noise and structured striping artifacts. Moreover, fine-grained textural details are well preserved without introducing noticeable artifacts.

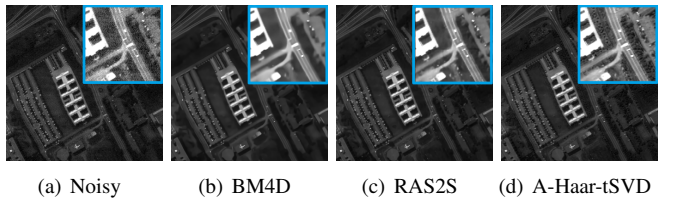


Fig. 20. Denoising comparison on the PaviaU data [99].

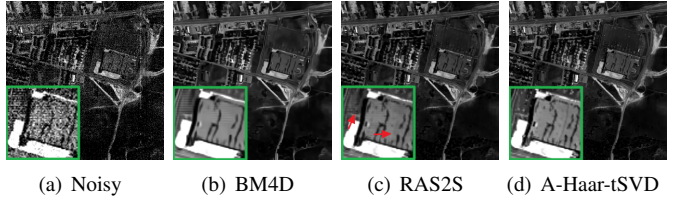


Fig. 21. Denoising comparison on the Urban data [100].

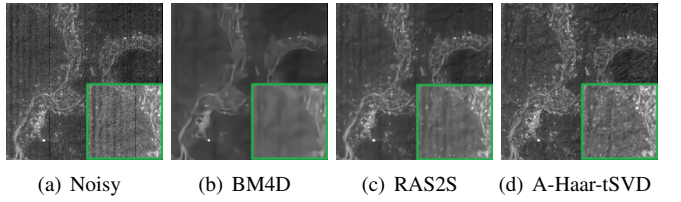


Fig. 22. Denoising comparison on the EO1 data [101].

E. Parameter Analysis

Following the classic patch-based denoising paradigm, the proposed Haar-tSVD transform relies on several key parameters such as the patch size ps , search window range W and number of nonlocal similar patches K . Fig. 23 evaluates the impact of these parameters on the denoising performance of Haar-tSVD across different datasets. For the patch size ps , a comparison between the CC15 and SIDD datasets shows that larger patch size can improve robustness against heavy noise contamination. However, increasing ps may drastically raise computational burden. Similarly, expanding the search range W and choosing more grouped patches K do not guarantee performance enhancement due to the rare patch effect. Based on these observations, we mainly set $ps = 8$, $W = 18$ and $K = 32$ in our experiments to achieve a tradeoff between denoising performance and speed.

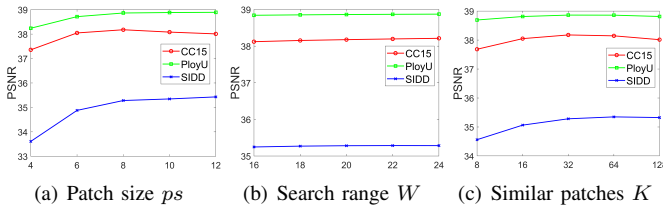


Fig. 23. Influence of different parameters on the Haar-tSVD transform.

F. Discussion

1) *Ablation study*: The effectiveness and robustness of the effective adaptive variant A-Haar-tSVD largely stems from the local adjustment of noise levels through eigenvalue analysis in Equ. (22). To further assess its impact, we conduct an ablation study. As shown in Table IX, A-Haar-tSVD consistently benefits from the adaptive noise level adjustment scheme in Equ. (23) across different scenarios, while incurring minimal computational cost, which justifies the efficiency and applicability of the proposed adaptive mechanism.

TABLE IX

COMPARISON OF THE PROPOSED A-HAAR-TSVD WITH AND WITHOUT LOCAL NOISE LEVEL ADJUSTMENT.

Dataset	Without local adjustment	With local adjustment
CC15	38.10/0.961	38.24/0.963
PolyU	38.77/0.969	38.89/0.971
HighISO	40.53/0.974	40.63/0.974
IOCI	41.39/0.977	41.52/0.978
SIDD-val	35.20/0.893	35.28/0.894
Time (s)	3.65	3.93

The adaptive variant A-Haar-tSVD introduces two weighting parameters, β and γ , which enhance robustness and adaptiveness based on the eigenvalue analysis in (22). We conduct a sensitivity study to evaluate the impact of β and γ , with the results presented in Fig. 24. We notice that a small $\beta (< 1)$ tends to overestimate the noise level, lead to oversmoothing and lower PSNR. On the other hand, choosing an excessively large γ may fail to capture the inner-group similarity under noisy conditions. Hence, a reasonable range for γ is between 12 and 16. Based on these findings, β and γ are empirically set to 1.2 and 13 in our experiments, respectively.

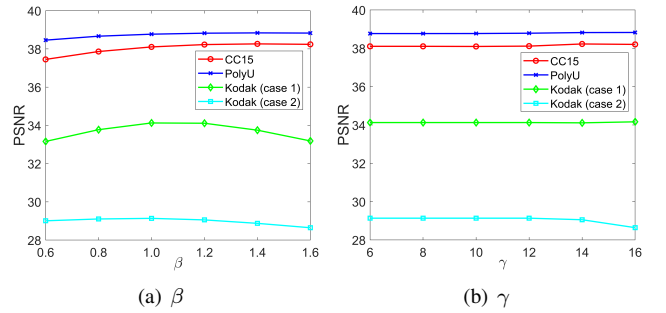


Fig. 24. Impact of weighting parameters β and γ on A-Haar-tSVD.

2) *Limitations and potential enhancement*: From Table IV, classic patch-based transforms struggle with severely-corrupted images, where noise energy may spread across all frequencies and all principal directions, thus the coefficients of noise overlap in magnitude with those of the true image. Hence, the thresholding operation fails to separate noise from signal. Beyond integrating DNNs with Haar-tSVD, it is interesting to devise an alternative approach within the patch-based paradigm to handle severe noise. Recently, Zontak et al. [102] observed that down-sampled noisy images contain patches with reduced noise and structures similar to clean ones. Therefore, instead of directly filtering the large-size noisy observation, an alternative is to first handle downsized image, and then restore the original resolution using image super-resolution techniques [103], [104].

V. CONCLUSION

In this paper, we present Haar-tSVD, an efficient and effective one-step method for image denoising. We leverage global and local circulant representation to capture similarity and correlation among image patches at both patch and group levels. Under the circulant formulation, we establish a theoretical connection between the Haar transform and PCA, and demonstrate that Haar-tSVD can be modeled by a unified t-SVD and Haar bases, resulting in a plug-and-play and parallelizable filtering approach. The proposed method reduces computational cost by avoiding the training of local transform bases. To achieve further acceleration, we also design and implement fast, parallelizable strategies. Moreover, we investigate the integration and combination of neural networks with the proposed Haar-tSVD. This leads to a flexible noise estimation scheme and an enhancement strategy based on the eigenvalue characteristics of circulant structures. The promising results motivate exploration of the proposed method and its adaptive scheme for broader applications in other imaging domains [105], [106].

REFERENCES

- [1] M. Elad, B. Kawar, and G. Vaksman, “Image denoising: The deep learning revolution and beyond—a survey paper,” *SIAM J. Imaging Sci.*, vol. 16, no. 3, pp. 1594–1654, 2023.
- [2] B. Wen, “Reproducible denoising methods,” [Online]. Available: <https://github.com/wenbihan/reproducible-image-denoising-state-of-the-art>.
- [3] K. Zhang, W. Zuo, Y. Chen, D. Meng, and L. Zhang, “Beyond a gaussian denoiser: Residual learning of deep cnn for image denoising,” *IEEE Trans. Image Process.*, vol. 26, no. 7, pp. 3142–3155, 2017.
- [4] S. Ioffe and C. Szegedy, “Batch normalization: Accelerating deep network training by reducing internal covariate shift,” in *Proc. Int. Conf. Mach. Learn.*, 2015, pp. 448–456.

[5] V. Nair and G. E. Hinton, "Rectified linear units improve restricted boltzmann machines," in *Proc. Int. Conf. Mach. Learn.*, 2010, pp. 807–814.

[6] K. He, X. Zhang, S. Ren, and J. Sun, "Deep residual learning for image recognition," in *Proc. IEEE Conf. Comput. Vis. Pattern Recognit.*, 2016, pp. 770–778.

[7] L. Chen, X. Chu, X. Zhang, and J. Sun, "Simple baselines for image restoration," in *Eur. Conf. Comput. Vis.* Springer, 2022, pp. 17–33.

[8] S. W. Zamir, A. Arora, S. Khan, M. Hayat, F. S. Khan, and M.-H. Yang, "Restormer: Efficient transformer for high-resolution image restoration," in *Proc. IEEE Conf. Comput. Vis. Pattern Recognit.*, 2022, pp. 5728–5739.

[9] A. Vaswani, N. Shazeer, N. Parmar, J. Uszkoreit, L. Jones, A. N. Gomez, Ł. Kaiser, and I. Polosukhin, "Attention is all you need," *Proc. Advances Neural Inf. Process. Syst.*, vol. 30, 2017.

[10] Z. Kong, F. Deng, H. Zhuang, X. Yang, J. Yu, and L. He, "A comparison of image denoising methods," *arXiv preprint arXiv:2304.08990*, 2023.

[11] V. Katkovnik, A. Foi, K. Egiazarian, and J. Astola, "From local kernel to nonlocal multiple-model image denoising," *Int. J. Comput. Vis.*, vol. 86, no. 1, pp. 1–32, 2010.

[12] D. Zoran and Y. Weiss, "From learning models of natural image patches to whole image restoration," in *Proc. IEEE Int. Conf. Comput. Vis.*, 2011, pp. 479–486.

[13] K. Dabov, A. Foi, V. Katkovnik, and K. Egiazarian, "Image denoising by sparse 3-d transform-domain collaborative filtering," *IEEE Trans. Image Process.*, vol. 16, no. 8, pp. 2080–2095, 2007.

[14] A. Buades, B. Coll, and J.-M. Morel, "A review of image denoising algorithms, with a new one," *Multiscale Model. Simul.*, vol. 4, no. 2, pp. 490–530, 2005.

[15] M. Elad and M. Aharon, "Image denoising via sparse and redundant representations over learned dictionaries," *IEEE Trans. Image Process.*, vol. 15, no. 12, pp. 3736–3745, 2006.

[16] L. P. Yaroslavsky, K. O. Egiazarian, and J. T. Astola, "Transform domain image restoration methods: review, comparison, and interpretation," in *Proc. Nonlinear Image Process. Pattern Anal. XII*, vol. 4304, 2001, pp. 155–169.

[17] S. Gu, L. Zhang, W. Zuo, and X. Feng, "Weighted nuclear norm minimization with application to image denoising," in *Proc. IEEE Conf. Comput. Vis. Pattern Recognit.*, 2014, pp. 2862–2869.

[18] J. Xu, L. Zhang, and D. Zhang, "A trilateral weighted sparse coding scheme for real-world image denoising," in *Eur. Conf. Comput. Vis.*, 2018, pp. 20–36.

[19] K. P. Murphy, *Machine learning: a probabilistic perspective*. MIT press, 2012.

[20] A. Lucas, M. Iliadis, R. Molina, and A. K. Katsaggelos, "Using deep neural networks for inverse problems in imaging: beyond analytical methods," *IEEE Signal Process. Mag.*, vol. 35, no. 1, pp. 20–36, 2018.

[21] G. J. Tee, "Eigenvectors of block circulant and alternating circulant matrices," *N. Z. J. Math.*, vol. 36, no. 8, pp. 195–211, 2007.

[22] Z. Zhang and S. Aeron, "Exact tensor completion using t-svd," *IEEE Trans. Signal Process.*, vol. 65, no. 6, pp. 1511–1526, 2016.

[23] T. G. Kolda and B. W. Bader, "Tensor decompositions and applications," *SIAM Rev.*, vol. 51, no. 3, pp. 455–500, 2009.

[24] A. Foi, V. Katkovnik, and K. Egiazarian, "Pointwise shape-adaptive det for high-quality denoising and deblocking of grayscale and color images," *IEEE Trans. Image Process.*, vol. 16, no. 5, pp. 1395–1411, 2007.

[25] A. Buades, J.-L. Lisani, and M. Miladinović, "Patch-based video denoising with optical flow estimation," *IEEE Trans. Image Process.*, vol. 25, no. 6, pp. 2573–2586, 2016.

[26] Y. Mäkinen, L. Azzari, and A. Foi, "Collaborative filtering of correlated noise: Exact transform-domain variance for improved shrinkage and patch matching," *IEEE Trans. Image Process.*, 2020.

[27] F. Chen, X. Zeng, and M. Wang, "Image denoising via local and nonlocal circulant similarity," *J. Vis. Commun. Image Represent.*, vol. 30, pp. 117–124, 2015.

[28] Z. Kong and X. Yang, "Color image and multispectral image denoising using block diagonal representation," *IEEE Trans. Image Process.*, vol. 28, no. 9, pp. 4247–4259, 2019.

[29] M. E. Kilmer and C. D. Martin, "Factorization strategies for third-order tensors," *Linear Algebra Appl.*, vol. 435, no. 3, pp. 641–658, 2011.

[30] M. E. Kilmer, K. Braman, N. Hao, and R. C. Hoover, "Third-order tensors as operators on matrices: A theoretical and computational framework with applications in imaging," *SIAM J. Matrix Anal. Appl.*, vol. 34, no. 1, pp. 148–172, 2013.

[31] G. M. PD, B. Madathil, and S. N. George, "Entropy-based reweighted tensor completion technique for video recovery," *IEEE Trans. Circuit Syst. Video Technol.*, vol. 30, no. 2, pp. 415–426, 2019.

[32] J. Xue, Y.-Q. Zhao, T. Wu, and J. C.-W. Chan, "Tensor convolution-like low-rank dictionary for high-dimensional image representation," *IEEE Trans. Circuit Syst. Video Technol.*, vol. 34, no. 12, pp. 13 257–13 270, 2024.

[33] J. A. Bengua, H. N. Phien, H. D. Tuan, and M. N. Do, "Efficient tensor completion for color image and video recovery: Low-rank tensor train," *IEEE Trans. Image Process.*, vol. 26, no. 5, pp. 2466–2479, 2017.

[34] T. Blu and F. Luisier, "The sure-let approach to image denoising," *IEEE Trans. Image Process.*, vol. 16, no. 11, pp. 2778–2786, 2007.

[35] Y. Hou, J. Xu, M. Liu, G. Liu, L. Liu, F. Zhu, and L. Shao, "Nlh: A blind pixel-level non-local method for real-world image denoising," *IEEE Trans. Image Process.*, vol. 29, pp. 5121–5135, 2020.

[36] Roeser and Jernigan, "Fast haar transform algorithms," *IEEE Trans. Comput.*, vol. 100, no. 2, pp. 175–177, 1982.

[37] S. Guo, Z. Liang, and L. Zhang, "Joint denoising and demosaicking with green channel prior for real-world burst images," *IEEE Trans. Image Process.*, vol. 30, pp. 6930–6942, 2021.

[38] Z. Kong, F. Deng, and X. Yang, "Image denoising using green channel prior," *IEEE Trans. Image Process.*, 2025.

[39] S. Nam, Y. Hwang, Y. Matsushita, and S. Joo Kim, "A holistic approach to cross-channel image noise modeling and its application to image denoising," in *Proc. IEEE Conf. Comput. Vis. Pattern Recognit.*, 2016, pp. 1683–1691.

[40] H. Yue, J. Liu, J. Yang, T. Q. Nguyen, and F. Wu, "High iso jpeg image denoising by deep fusion of collaborative and convolutional filtering," *IEEE Trans. Image Process.*, vol. 28, no. 9, pp. 4339–4353, 2019.

[41] A. Abdelhamed, S. Lin, and M. S. Brown, "A high-quality denoising dataset for smartphone cameras," in *Proc. IEEE Conf. Comput. Vis. Pattern Recognit.*, 2018, pp. 1692–1700.

[42] Z. Wang, A. C. Bovik, H. R. Sheikh, and E. P. Simoncelli, "Image quality assessment: from error visibility to structural similarity," *IEEE Trans. Image Process.*, vol. 13, no. 4, pp. 600–612, 2004.

[43] L. Zhang, W. Dong, D. Zhang, and G. Shi, "Two-stage image denoising by principal component analysis with local pixel grouping," *Pattern Recognit.*, vol. 43, no. 4, pp. 1531–1549, 2010.

[44] Q. Guo, C. Zhang, Y. Zhang, and H. Liu, "An efficient svd-based method for image denoising," *IEEE Trans. Circuit Syst. Video Technol.*, vol. 26, no. 5, pp. 868–880, 2015.

[45] D. L. Donoho and J. M. Johnstone, "Ideal spatial adaptation by wavelet shrinkage," *biometrika*, vol. 81, no. 3, pp. 425–455, 1994.

[46] X. Gong, W. Chen, and J. Chen, "A low-rank tensor dictionary learning method for hyperspectral image denoising," *IEEE Trans. Signal Process.*, vol. 68, pp. 1168–1180, 2020.

[47] Q. Shi, Y.-M. Cheung, and J. Lou, "Robust tensor svd and recovery with rank estimation," *IEEE Trans. Cybern.*, vol. 52, no. 10, pp. 10 667–10 682, 2022.

[48] H. C. Burger, C. J. Schuler, and S. Harmeling, "Image denoising: Can plain neural networks compete with bm3d?" in *Proc. IEEE Conf. Comput. Vis. Pattern Recognit.*, 2012, pp. 2392–2399.

[49] L. P. Yaroslavsky, "Local adaptive image restoration and enhancement with the use of dft and dct in a running window," in *Proc. SPIE*, vol. 2825, 1996, pp. 2–13.

[50] J. Xu, L. Zhang, D. Zhang, and X. Feng, "Multi-channel weighted nuclear norm minimization for real color image denoising," in *Proc. IEEE Int. Conf. Comput. Vis.*, 2017, pp. 1096–1104.

[51] J. Xu, L. Zhang, and D. Zhang, "External prior guided internal prior learning for real-world noisy image denoising," *IEEE Trans. Image Process.*, vol. 27, no. 6, pp. 2996–3010, 2018.

[52] G. Treece, "Real image denoising with a locally-adaptive bitonic filter," *IEEE Trans. Image Process.*, vol. 31, pp. 3151–3165, 2022.

[53] M. Maggioni, V. Katkovnik, K. Egiazarian, and A. Foi, "Nonlocal transform-domain filter for volumetric data denoising and reconstruction," *IEEE Trans. Image Process.*, vol. 22, no. 1, pp. 119–133, 2012.

[54] A. Rajwade, A. Rangarajan, and A. Banerjee, "Image denoising using the higher order singular value decomposition," *IEEE Trans. Pattern Anal. Mach. Intell.*, vol. 35, no. 4, pp. 849–862, 2012.

[55] Y. Peng, D. Meng, Z. Xu, C. Gao, Y. Yang, and B. Zhang, "De-composable nonlocal tensor dictionary learning for multispectral image denoising," in *Proc. IEEE Conf. Comput. Vis. Pattern Recognit.*, 2014, pp. 2949–2956.

[56] Y. Chang, L. Yan, and S. Zhong, "Hyper-laplacian regularized unidirectional low-rank tensor recovery for multispectral image denoising," in *Proc. IEEE Conf. Comput. Vis. Pattern Recognit.*, 2017, pp. 4260–4268.

[57] PyTorch Team, Training a classifier. [Online]. Available: https://docs.pytorch.org/tutorials/beginner/blitz/cifar10_tutorial.html

[58] Kodak, “Kodak gallery dataset,” [Online]. Available: <http://r0k.us/graphics/kodak>.

[59] T. Plotz and S. Roth, “Benchmarking denoising algorithms with real photographs,” in *Proc. IEEE Conf. Comput. Vis. Pattern Recognit.*, 2017, pp. 1586–1595.

[60] J. Xu, H. Li, Z. Liang, D. Zhang, and L. Zhang, “Real-world noisy image denoising: A new benchmark,” *arXiv preprint arXiv:1804.02603*, 2018.

[61] K. Dabov, A. Foi, V. Katkovnik, and K. Egiazarian, “Color image denoising via sparse 3d collaborative filtering with grouping constraint in luminance-chrominance space,” in *Proc. IEEE Int. Conf. Image Process.*, 2007, pp. 313–316.

[62] Q. Ma, J. Jiang, X. Zhou, P. Liang, X. Liu, and J. Ma, “Pixel2pixel: A pixelwise approach for zero-shot single image denoising,” *IEEE Trans. Pattern Anal. Mach. Intell.*, 2025.

[63] H. Kim and N. I. Cho, “Apr-rd: Complemental two steps for self-supervised real image denoising,” in *Proc. AAAI*, vol. 39, no. 4, 2025, pp. 4257–4265.

[64] Z. Wang, J. Liu, G. Li, and H. Han, “Blind2unblind: Self-supervised image denoising with visible blind spots,” in *Proc. IEEE Conf. Comput. Vis. Pattern Recognit.*, 2022, pp. 2027–2036.

[65] S. Herbreteau and M. Unser, “Self-calibrated variance-stabilizing transformations for real-world image denoising,” 2025.

[66] J. Li, Z. Zhang, X. Liu, C. Feng, X. Wang, L. Lei, and W. Zuo, “Spatially adaptive self-supervised learning for real-world image denoising,” in *Proc. IEEE Conf. Comput. Vis. Pattern Recognit.*, 2023.

[67] J. Li, Z. Zhang, and W. Zuo, “Rethinking transformer-based blind-spot network for self-supervised image denoising,” *arXiv preprint arXiv:2404.07846*, 2024.

[68] Y. Quan, T. Zheng, Z. Ma, and H. Ji, “Zero-shot blind-spot image denoising via implicit neural sampling,” in *IEEE Conf. Comput. Vis. Pattern Recog.*, 2025, pp. 7502–7512.

[69] J. Cheng, D. Liang, and S. Tan, “Transfer clip for generalizable image denoising,” in *IEEE Conf. Comput. Vis. Pattern Recog.*, 2024, pp. 25974–25984.

[70] Y. Huang and H. Huang, “Beyond image prior: Embedding noise prior into conditional denoising transformer,” *arXiv preprint arXiv:2407.09094*, 2024.

[71] X. Deng, C. Zhang, L. Jiang, J. Xia, and M. Xu, “Deepsn-net: Deep semi-smooth newton driven network for blind image restoration,” *IEEE Trans. Pattern Anal. Mach. Intell.*, 2025.

[72] S. Yu, B. Park, and J. Jeong, “Deep iterative down-up cnn for image denoising,” in *Proc. Conf. Comput. Vis. Pattern Recognit. Workshops*, 2019.

[73] T. Li, H. Feng, L. Wang, L. Zhu, Z. Xiong, and H. Huang, “Stimulating diffusion model for image denoising via adaptive embedding and ensembling,” *IEEE Trans. Pattern Anal. Mach. Intell.*, 2024.

[74] K. Zhang, W. Zuo, and L. Zhang, “Ffdnet: Toward a fast and flexible solution for cnn-based image denoising,” *IEEE Trans. Image Process.*, vol. 27, no. 9, pp. 4608–4622, 2018.

[75] D. Kim, J. Ko, M. K. Ali, and T. H. Kim, “Idf: Iterative dynamic filtering networks for generalizable image denoising,” in *Int. Conf. Comput. Vis.*, 2025.

[76] B. Li, H. Zhao, W. Wang, P. Hu, Y. Gou, and X. Peng, “Mair: A locality- and continuity-preserving mamba for image restoration,” in *IEEE Conf. Comput. Vis. Pattern Recog.*, Nashville, TN, Jun. 2025.

[77] M. Maggioni, G. Boracchi, A. Foi, and K. Egiazarian, “Video denoising, deblocking, and enhancement through separable 4-d nonlocal spatiotemporal transforms,” *IEEE Trans. Image Process.*, vol. 21, no. 9, pp. 3952–3966, 2012.

[78] B. Wen, S. Ravishankar, and Y. Bresler, “Vidosat: High-dimensional sparsifying transform learning for online video denoising,” *IEEE Trans. Image Process.*, vol. 28, no. 4, pp. 1691–1704, 2018.

[79] A. Davy, T. Ehret, J.-M. Morel, P. Arias, and G. Facciolo, “A non-local cnn for video denoising,” in *Proc. IEEE Conf. Int. Image Process.*, 2019, pp. 2409–2413.

[80] M. Tassano, J. Delon, and T. Veit, “Dvdnet: A fast network for deep video denoising,” in *Proc. IEEE Conf. Int. Image Process.*, 2019, pp. 1805–1809.

[81] ——, “Fastdvdnet: Towards real-time deep video denoising without flow estimation,” in *Proc. IEEE Conf. Comput. Vis. Pattern Recognit.*, June 2020.

[82] J. Li, X. Wu, Z. Niu, and W. Zuo, “Unidirectional video denoising by mimicking backward recurrent modules with look-ahead forward ones,” in *Eur. Conf. Comput. Vis.* Springer, 2022, pp. 592–609.

[83] Z. Chen, T. Jiang, X. Hu, W. Zhang, H. Li, and H. Wang, “Spatiotemporal blind-spot network with calibrated flow alignment for self-supervised video denoising,” in *Proc. AAAI*, vol. 39, no. 3, 2025, pp. 2411–2419.

[84] D. Y. Sheth, S. Mohan, J. L. Vincent, R. Manzorro, P. A. Crozier, M. M. Khapra, E. P. Simoncelli, and C. Fernandez-Granda, “Unsupervised deep video denoising,” in *Proc. IEEE Int. Conf. Comput. Vis.*, 2021, pp. 1759–1768.

[85] M. Claus and J. Van Gemert, “Videnn: Deep blind video denoising,” in *Proc. Conf. Comput. Vis. Pattern Recognit. Workshops*, 2019, pp. 0–0.

[86] J. Liang, J. Cao, Y. Fan, K. Zhang, R. Ranjan, Y. Li, R. Timofte, and L. Van Gool, “Vrt: A video restoration transformer,” *IEEE Trans. Image Process.*, 2024.

[87] H. Yue, C. Cao, L. Liao, R. Chu, and J. Yang, “Supervised raw video denoising with a benchmark dataset on dynamic scenes,” in *Proc. IEEE Conf. Comput. Vis. Pattern Recognit.*, 2020, pp. 2301–2310.

[88] W. He, Q. Yao, C. Li, N. Yokoya, and Q. Zhao, “Non-local meets global: An integrated paradigm for hyperspectral denoising,” in *Proc. IEEE Conf. Comput. Vis. Pattern Recognit.*, 2019, pp. 6861–6870.

[89] J.-L. Zhao, T.-H. Zhang, S. Fang, J.-F. Gao, J.-Y. Wang, and M.-G. Gong, “Spatial-spectral texture-preserved total variation: A novel regularization for hyperspectral image denoising,” *IEEE Trans. Circuit Syst. Video Technol.*, 2025.

[90] Y. Chen, H. Zhang, Y. Wang, Y. Yang, and J. Wu, “Flex-dld: Deep low-rank decomposition model with flexible priors for hyperspectral image denoising and restoration,” *IEEE Trans. Image Process.*, 2024.

[91] Y. Chang, L. Yan, H. Fang, S. Zhong, and W. Liao, “Hsi-denet: Hyperspectral image restoration via convolutional neural network,” *IEEE Trans. Geosci. Remote Sens.*, vol. 57, no. 2, pp. 667–682, 2018.

[92] F. Xiong, J. Zhou, Q. Zhao, J. Lu, and Y. Qian, “Mac-net: Model-aided nonlocal neural network for hyperspectral image denoising,” *IEEE Trans. Geosci. Remote Sens.*, vol. 60, pp. 1–14, 2021.

[93] K. Wei, Y. Fu, J. Yang, and H. Huang, “A physics-based noise formation model for extreme low-light raw denoising,” in *Proc. IEEE Conf. Comput. Vis. Pattern Recognit.*, 2020, pp. 2758–2767.

[94] J. Xiao, Y. Liu, and X. Wei, “Region-aware sequence-to-sequence learning for hyperspectral denoising,” in *Eur. Conf. Comput. Vis.* Springer, 2024, pp. 218–235.

[95] A. Maffei, J. M. Haut, M. E. Paoletti, J. Plaza, L. Bruzzone, and A. Plaza, “A single model cnn for hyperspectral image denoising,” *IEEE Trans. Geosci. Remote Sens.*, vol. 58, no. 4, pp. 2516–2529, 2019.

[96] R. H. Yuhas, J. W. Boardman, and A. F. Goetz, “Determination of semi-arid landscape endmembers and seasonal trends using convex geometry spectral unmixing techniques,” *ratio*, vol. 4, p. 22, 1990.

[97] L. Wald, *Data fusion: definitions and architectures: fusion of images of different spatial resolutions*. Les Presses de l’Ecole des Mines, 2002.

[98] J. Song, J.-H. Jeong, D.-S. Park, H.-H. Kim, D.-C. Seo, and J. C. Ye, “Unsupervised denoising for satellite imagery using wavelet directional cyclegan,” *IEEE Trans. Geosci. Remote Sens.*, vol. 59, no. 8, pp. 6823–6839, 2020.

[99] https://www.ehu.eus/ccwintco/index.php/Hyperspectral_Remote_Sensing_Scenes.

[100] L. S. Kalman and E. M. Bassett III, “Classification and material identification in an urban environment using hydice hyperspectral data,” in *Imaging Spectrometry III*, vol. 3118. SPIE, 1997, pp. 57–68.

[101] E. M. Middleton, S. G. Ungar, D. J. Mandl, L. Ong, S. W. Frye, P. E. Campbell, D. R. Landis, J. P. Young, and N. H. Pollack, “The earth observing one (eo-1) satellite mission: Over a decade in space,” *IEEE J. Sel. Top. Appl. Earth Obs. Remote. Sens.*, vol. 6, no. 2, pp. 243–256, 2013.

[102] M. Zontak, I. Mosseri, and M. Irani, “Separating signal from noise using patch recurrence across scales,” in *Proc. IEEE Conf. Comput. Vis. Pattern Recognit.*, 2013, pp. 1195–1202.

[103] C. Dong, C. C. Loy, K. He, and X. Tang, “Image super-resolution using deep convolutional networks,” *IEEE Trans. Pattern Anal. Mach. Intell.*, vol. 38, no. 2, pp. 295–307, 2015.

[104] Z. Wang, J. Chen, and S. C. Hoi, “Deep learning for image super-resolution: A survey,” *IEEE Trans. Pattern Anal. Mach. Intell.*, 2020.

[105] H. Fu, J. Liang, Z. Fang, J. Han, F. Liang, and G. Zhang, “Weconvne: Learned image compression with wavelet-domain convolution and entropy model,” in *Eur. Conf. Comput. Vis.* Springer, 2024, pp. 37–53.

[106] Y. Luo, X. Zhao, and D. Meng, “Revisiting nonlocal self-similarity from continuous representation,” *IEEE Trans. Pattern Anal. Mach. Intell.*, 2024.